# Photonic Weyl points due to broken time-reversal symmetry in magnetized semiconductor

Dongyang Wang[1,2†], Biao Yang[1,3†], Wenlong Gao[1], Hongwei Jia[1], Quanlong Yang[2], Xieyu Chen[2], Minggui Wei[2], Changxu Liu[1], Miguel Navarro-Cía[1], Jiaguang Han[2*], Weili Zhang[2, 4*], Shuang Zhang[1*]

1. School of Physics & Astronomy, University of Birmingham, Birmingham, B15 2TT, UK
2. Center for Terahertz Waves and College of Precision Instrument and Optoelectronics Engineering, Tianjin University and the Key Laboratory of Optoelectronics Information and Technology (Ministry of Education), Tianjin 300072, China.
3. College of Advanced Interdisciplinary Studies, National University of Defense Technology, Changsha 410073, China.
4. School of Electrical and Computer Engineering, Oklahoma State University, Stillwater, Oklahoma 74078, USA

*Correspondence to: jiaghan@tju.edu.cn; wwzhang@okstate.edu; s.zhang@bham.ac.uk

†These authors contributed equally to this work.

**Weyl points are discrete locations in the three-dimensional momentum space where two bands cross linearly with each other. They serve as the monopoles of Berry curvature in the momentum space, and their existence requires breaking of either time-reversal or inversion symmetry[1-16]. Although various non-centrosymmetric Weyl systems have been reported[15], demonstration of Weyl degeneracies due to breaking of the time reversal symmetry remains scarce and is limited to electronic systems[17,18]. Here, we report the experimental observation of photonic Weyl degeneracies in a magnetized semiconductor - InSb, which behaves as magnetized plasma[19] for electromagnetic waves at the terahertz band. By varying the magnetic field strength, Weyl points and the corresponding photonic Fermi-arcs have been demonstrated.**

**Our observation establishes magnetized semiconductors as a reconfigurable[20] terahertz Weyl system, which may prompt research on novel magnetic topological phenomena such as chiral Majorana type edge states and zero modes in classic systems[21,22].**

Weyl points as topologically chiral singularity points in the three-dimensional momentum space have been extensively investigated in both quantum and classical systems[15]. In photonics, Weyl points have been observed in various systems such as gyroid photonic crystals[7,23], metamaterials[24-26], and evanescently coupled helical waveguides[27]. However, all the previously demonstrated photonic Weyl points are exclusively based on systems with broken inversion symmetry[15]. On the other hand, it has been proposed that Weyl points due to breaking of the time-reversal symmetry may possess more interesting properties such as axial anomaly, giant photocurrent and novel quantum oscillation phenomena[28-30]. They may enable multiple striking topological features such as Majorana type edge states and zero mode[22], which do not exist in inversion symmetry breaking systems. Although there have been theoretical proposals on implementation of Weyl degeneracies by applying external magnetic fields on finely designed photonic crystals[16,31], very few of them are easily realizable in experiment due to the challenge in three-dimensional structuring of magnetic materials[32,33]. Interestingly, it was recently theoretically proposed that plasma, the fourth fundamental state of natural matter[34,35], can support Weyl degeneracies under external magnetic fields[19], as well as nonreciprocal wave transport[36-38]. Since there is no structuring involved, this represents a facile and tunable approach for achieving photonic Weyl degeneracies arising from time-reversal symmetry breaking.

In this work, by applying magnetic field to intrinsic semiconductor InSb, we demonstrate photonic Weyl points due to broken time reversal symmetry. Here InSb[39,40] is chosen because of its very small effective mass of electrons ($m^* = 0.015m_0$, where $m_0$ is the free electron mass) that can lead to a terahertz cyclotron frequency under a moderate applied magnetic field. Along the direction of magnetic field, electrons can move freely. Therefore, the dielectric function is described by the Drude model, and there exists a longitudinal bulk plasma mode along the applied magnetic field. However, in the plane perpendicular to the magnetic field, the dielectric function is significantly modified due to the cyclotron motion of electrons, which leads to the breaking of degeneracy between the left and right circular polarizing (L/RCP) modes propagating along the magnetic field[40,36]. The linear crossing between the longitudinal plasma mode and a circular polarizing mode forms a Weyl point in the magnetized plasma system[19]. By considering the coupling between the electromagnetic wave and the motion of the free charges in the plasma, we can derive a full Hamiltonian $H$ as (see supplementary information 1)[19]:

$$\omega_p \begin{bmatrix} 0 & -k\times/\sqrt{\varepsilon_\infty}k_p & -i/\sqrt{\varepsilon_\infty} \\ k\times/\sqrt{\varepsilon_\infty}k_p & 0 & 0 \\ i\sqrt{\varepsilon_\infty} & 0 & (\omega_c\Delta - i\gamma I)/\omega_p \end{bmatrix} \begin{bmatrix} E \\ H \\ V \end{bmatrix} = \omega \begin{bmatrix} E \\ H \\ V \end{bmatrix} \quad (1)$$

where $\omega_p = \sqrt{ne^2/\varepsilon_0\varepsilon_\infty m^*}$ and $\omega_c = eB/m^*$ are the plasma frequency and electron cyclotron frequency, respectively, with $n$ being the free electron density, $\varepsilon_0$ the permittivity of vacuum and $\varepsilon_\infty = 16$ the dielectric constant at high frequencies; $k_p$ is the vacuum wave vector at the plasma frequency, $\gamma$ is the damping frequency and $\Delta = [\sigma_y, 0 ; 0, 0]$ with $\sigma_y$ being the second Pauli matrix. By carefully controlling the temperature, the carrier density of InSb can be tuned to give a plasma frequency around $\omega_p/2\pi = 0.3$ THz, which falls in the frequency range of our terahertz measurement setup. Depending on the relative values of $\omega_c$ and $\omega_p$, different numbers of Weyl points may show up in our system (see supplementary information 2, Fig. S1). When $\omega_c > \omega_p$, there are two pairs of Weyl points appearing at the plasma frequency with the momentum coordinates $(k_x, k_y, k_z) = (0, 0, \pm\sqrt{\varepsilon_\infty\omega_c/(\omega_c \pm \omega_p)})$, where the magnetic field is applied along z direction. Around the outer Weyl point (located at larger $k_z$), the first order $k{\cdot}p$ Hamiltonian expansion can be expressed as:

$$H_1 = \frac{N}{2}(\sigma_0 + \sigma_3)(M\delta k_z + \xi P\delta B) + N\sigma_1\delta k_y - N\sigma_2\delta k_x \quad (2)$$

with parameters $M$, $N$, $P$ being linear dispersion coefficients defined by the coordinates at the outer Weyl point, $\xi$ the cyclotron constant and $\sigma_i$ the Pauli matrices as described in supplementary information 3.

For a semiconductor InSb under a magnetic field strength of $B = 0.19$ T, the corresponding cyclotron frequency is $\omega_c/2\pi \approx 0.35$ THz, which leads to the band structure shown in Fig. 1a, where plasma frequency is taken as $\omega_p/2\pi = 0.31$ THz. Along the magnetic field, four double degenerate Weyl points are located at the plasma frequency as expected. Here, we only consider the outer pair of Weyl points as the inner pair with opposite topological charges are enclosed by the same equifrequency surface and therefore they are not responsible for the observed topological features. Fig. 1b shows the projected band structure around one of the outer Weyl points. It is shown that the dispersions of two participating modes divide the momentum-energy space into four regions representing the bulk states and gaps, respectively. This projected band morphology as a signature of photonic Weyl points can be observed through the reflection spectra when scanning the wave vector $k_z$. However, in the experiment, scanning $k_z$ requires an angle resolved reflection system, which is incompatible with our magnetic terahertz system. Equivalently, we can scan the magnetic field strength $B$ instead of $k_z$, since they behave similarly in constructing the parameter space of the Weyl point, as shown by the form of effective Hamiltonian in Eq. 2. Fig. 1c shows the band structure constructed in the synthetic parameter space [$k_x$, $k_y$, $B$] for a fixed incident wave vector of $k_z = 2\pi/90\ \mu m^{-1}$. One can see that the linear crossing is preserved in the substituted band structure (Fig. 1d, e), confirming the presence of Weyl points in the synthetic parameter space (for detailed proof, see supplementary information 3).

In order to characterize the Weyl point, we apply a magnetic field along an in-plane direction (parallel to the surface), as shown in Fig. 2a. It is expected that two Weyl points of opposite chiralities appear along the direction of $B$ field. They are both located outside the light cone. In order to probe the reflection spectra around the Weyl points, we employ a grating to compensate the in-plane momentum mismatch between the incident terahertz wave and the Weyl points. The aluminum grating, fabricated directly on the surface of the InSb wafer, has a period of $p = 90\ \mu m$, a filling ratio of 2/3 and a thickness of $t = 1\ \mu m$. The sample is then placed in a low temperature environment of $T = 50$ K to provide a plasma frequency of $\omega_p/2\pi \approx 0.31$ THz with a damping factor of $\gamma/2\pi = 3\times10^{10}$ Hz. A normal incidence configuration is employed with the magnetic field applied along the grating direction, as shown in Fig. 2b. A high resistivity float zone Silicon 50/50 terahertz beam splitter is used for the reflection spectra measurement. The grating provides a fundamental order wave vector of magnitude $G = 2\pi/p$ to excite both the bulk and surface states supported by the magnetized InSb. As the magnetic field strength is scanned from 0-1 Tesla, we measure the reflection spectrum. These measurements provide the projected band information as shown in Fig. 2c, where the band crossing can be clearly observed at the frequency of $\omega_p/2\pi$ = 0.31 THz and magnetic field of $B$ = 0.19 T. Fig. 2d shows the corresponding full wave simulation results that take into account the actual dissipation in the magnetized plasma. Simulation results shown in Fig. 2d show good agreement with the experimental results. On the other hand, when the grating direction is rotated away from the direction of magnetic field, the crossing point disappears and a bandgap is formed, as shown in supplementary information 4, Fig. S2. The experimental results confirm the presence of Weyl degeneracies in a magnetized semiconductor system.

The most important signature of a Weyl system is the presence of Fermi-arcs. The photonics Fermi-arcs in the original momentum space are explored in the supplementary information 5 where the surface states are found to be separated into two separated frequency bands: $\omega < \omega_p$ and $\omega > \sqrt{\omega_p^2 + \omega_c^2}$ with opposite signs of $k_y$, respectively, due to the magnetic field induced cyclotron resonance. These two branches of surface states are observed in the experimentally measured *f*-*B* plot manifested as absorption lines in the reflection spectra. The theoretically calculated surface states are indicated by a black dashed line in both the experimental and simulated results in Fig. 2c-d, which fits well with the corresponding surface states induced absorption.

To further explore the surface state features in the magnetized Weyl system, a second experimental configuration is employed as shown in Fig. 3a, in which the incidence terahertz beam and the applied magnetic field are arranged to form angles $\theta = 45°$ and $\alpha = 45°$ with respect to the sample normal and sample surface, respectively. In this configuration, a beam splitter is not required and therefore the signal noise ratio of the measurement is improved by approximately four times in comparison to that of normal incidence. Rotating the grating around $x$ axis by an angle of $\varphi$ as shown in Fig. 3a (bottom-left inset) provides a non-zero $k_y$ to excite the off $k_z$ axis surface states on the $k_y$ - $k_z$ plane, as shown in Fig. 3a (right insets). Meanwhile, due to the tilted incidence, the degeneracy between $\pm 1^{st}$ grating order is lifted. The $\pm 1^{st}$ order excitation wave vector is given by $[k_y, k_z]_{\pm 1} = [\pm G \sin\varphi, \pm G \cos\varphi + k_0 \sin 45°]$ as illustrated in Fig. 3a (bottom-left inset), where $\varphi$ is the angle formed between the grating momentum and $z$ axis. For a given magnetic field, it is expected that the ±1st order with opposite signs of $k_y$ can excite surface states at the two aforementioned frequency bands (see supplementary information 5, Fig S3).

In this tilted configuration, the Weyl points are projected onto the sample surface with a smaller in-plane wave vector ($k_z=\pm\sqrt{\varepsilon_\infty\,\omega_c/2(\omega_c-\omega_p)}$), as shown in Fig. 3b. A different sample with a greater grating periodicity of $p$ = 120 μm is therefore designed to match the momentum. The new sample has a similar plasma frequency $\omega_p/2\pi \approx 0.31$ THz as the previous one. The projected bulk bands on $B-f$ plane are plotted for $\varphi$ = -30° and -45° in Fig. 3c and f, where the bulk states excited by the ±1st grating orders have a large overlap with each other and are indicated by navy and purple color, respectively. The surface states excited by the ±1st grating orders are also calculated and shown in Fig. 3c and f, respectively. At each grating angle $\varphi$, the ±1st order excitations with opposite signs of $k_y$ form two separate branches, which merge into each other at zero applied magnetic field B. It is also observed that at increasing $\varphi$, the angle between two surface state branches widens, due to the increase in the slopes of the dispersion. It can be noticed that the surface state is interrupted around the cyclotron position, which is caused by the strong cyclotron resonance that leads to relatively high reflection[41]. For a negative $\varphi$, the diffraction orders that excite the two surface state branches switch in comparison to that with a positive $\varphi$ (see more discussion in supplementary information 6, Fig. S4).

The measured reflection spectra are shown in Fig. 3e and Fig. 3h for $\varphi$ = -30° and -45° (see supplementary information 7, Fig. S5 for more measured results), respectively, which presents the superposed band projection for both bulk and surface states. The corresponding simulation results for the reflection spectra shown in Fig. 3d and g are in good agreement with the experiment results. It is noticed that there exists a cut-off for the surface state branch at higher frequencies, due to the limited momentum provided by the grating (see supplementary information 8, Fig. S6). Higher grating orders are also excited in the experiment, which contribute to the absorptions along the surface state branch at the higher frequencies beyond the cut-off of the first grating order.

For a given grating diffraction order, the projection of photonic Weyl point can also be described in the parameter space [$\varphi$, $B$]. Using the same configuration as in Fig. 3a, a sample with higher plasma frequency of $\omega_p/2\pi \approx 0.53$ THz and grating periodicity of $p$=150μm is measured (supplementary information 9, Fig. S7). The Weyl point which is projected at location ($k_y$, $k_z$) = (0, $G + k_0 \sin 45°$) in the momentum space turns into ($\varphi$, $B$) = (0, 0.472) for the +1 grating order (supplementary information 10, Fig. S8). The projected dispersion of the bulk states with respect to $B$ for $\varphi$ =0 is shown in Fig. 4a, where a linear crossing indicating an effective Weyl point is observed. The linear dispersion with respect to $\varphi$ around the effective Weyl point is confirmed in Fig. 4b. The calculated surface states for different grating orientation angle $\varphi$ are shown in Fig. 4c and d, where it is clearly shown that larger orientation angles lead to steeper dispersion in $B$. A photonic Fermi-arc in the $B$-$\varphi$ plane can thus be constructed at a given frequency. For the +1st grating order excitation, the photonic Fermi-arcs together with the bulk bands at two different frequencies 0.46 THz and 0.6 THz are shown in Fig. 4e and f, respectively. The experimental data (cyan hollow dots) is in good agreement with the theoretical result. It should be noted that due to the presence of loss, the Weyl point transforms into exceptional ring[19], which possesses the same topological charge as a Weyl point. The size of the ring is calculated based on the actual dissipation of the semiconductor and is found to be negligibly small (see supplementary information 11, Fig. S9). Meanwhile, a discussion of the loss and surface wave resonance is shown in supplementary information 12, Fig. S10.

In summary, we have demonstrated the first classical system possessing Weyl points due to time reversal symmetry breaking. The locations of the Weyl points can be readily tuned by varying the applied magnetic field or the temperature. Importantly, our Weyl system does not require complicated 3D fabrication as required by previously demonstrated classical Weyl systems. The observed Weyl points and topological surface states in the magnetized InSb also represent the first demonstration of topological phase in the terahertz band, which may facilitate the development of terahertz topological devices.

**Data availability:**

The data that support the findings of this study are available from the corresponding author on request.

**Acknowledgement:**

This work is supported by ERC Consolidator Grant (TOPOLOGICAL), the Royal Society and the Wolfson Foundation. M. N.-C. acknowledges support from University of Birmingham (Birmingham Fellowship).

**Figures:**

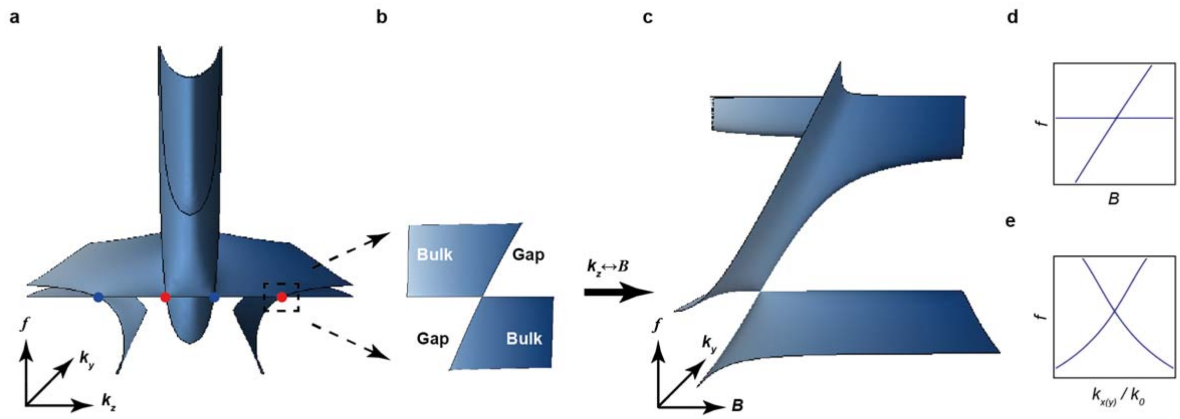


**Figure 1 | Bulk states of lossless magnetized InSb. a**, The band structure and Weyl points in magnetized plasma system. The parameters used in the calculation are: $\omega_p/2\pi = 0.31$ THz, $B = 0.19$ T and no damping is considered. **b**, Band projection around the outer Weyl point, whose coordinate is $(k_x, k_y, k_z) = (0, 0, 10.8)\ k_p$ with $k_p$ indicating the vacuum wave vector at plasma frequency. **c**, Band structure with $k_z$ been substituted by $B$. A fixed value of $k_z = 10.8\ k_p$ is assumed and the magnetic field scanning range is $0 \leq B \leq 1$T. **d**, Dispersion along $B$ around the outer Weyl point in **c**. **e**, Similar to **d** but along $k_{x(y)}$. $k_0$ indicates vacuum wave vector.

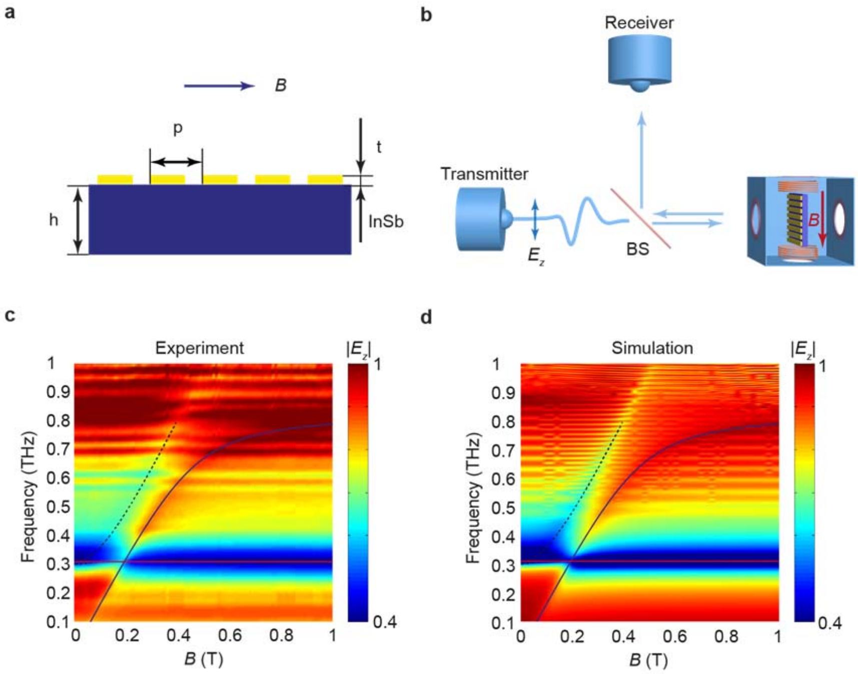


**Figure 2 | Observation of terahertz Weyl point in a magnetized semiconductor system. a**, Schematic of the sample with metal grating on top of the InSb substrate. The specified magnetic field direction is along grating, geometric parameters are: $p$ = 90 μm, $h$ = 1250 μm and $t$ = 1 μm. **b**, Illustration of the experiment setup for terahertz reflection measurement. Two terahertz antennas are placed to be right angle and form a normal incidence onto the sample. 'BS' indicates the 50/50 beam splitter. The sample is placed in a commercial equipment with low temperature environment, where the built in superconducting coils provide tunable magnetic field strength. Linear polarization of incidence wave is indicated. **c**, Experimentally measured reflection spectra. The band crossing coordinate can be estimated as $\omega_p/2\pi \approx 0.31$ THz and $B = 0.19$ T. **d**, Reflection spectra calculated with full wave simulation, a damping factor of $\gamma/2\pi = 3\times10^{10}$ Hz is considered in the simulation. ~~Dashed line indicates the cyclotron resonance position ($\omega_c/2\pi \approx 1.8626\times B$ THz)~~, red/blue curves are the bulk states and black curves are surface states under lossless assumption, respectively.

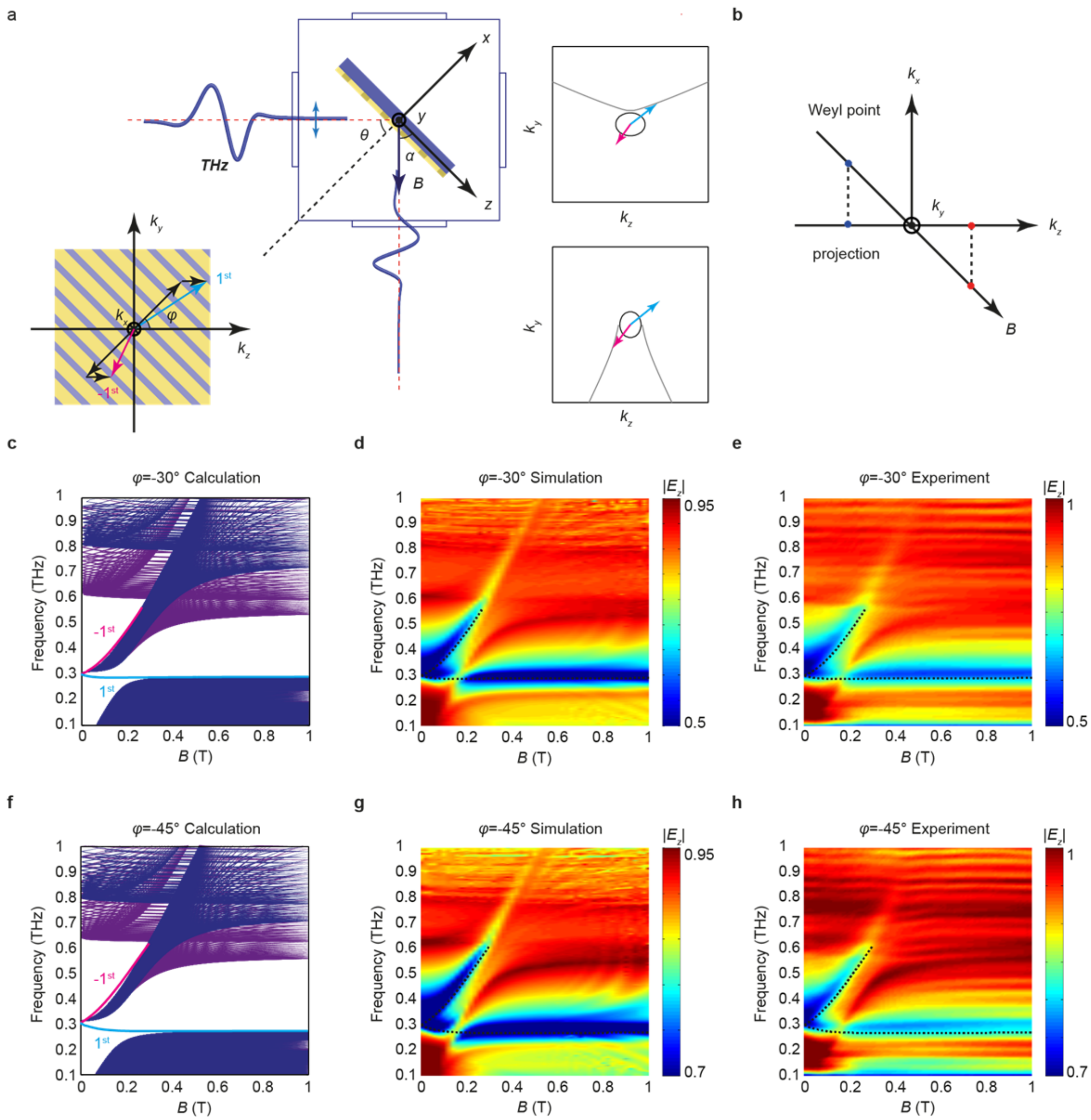


**Figure 3 | Surface states under tilted incidence excitation. a**, Schematic experiment configuration with respect of $\theta$=45° and $\alpha$=45°. The rotation angle of grating is $\varphi$ about $x$-axis. ±1st grating order momentum is coupled with incidence wave and excites surface states for corresponding grating angle $\varphi$. The material parameters for the sample are $\omega_p/2\pi \approx 0.31$ THz and $\gamma/2\pi = 3\times10^{10}$ Hz. **b**, Projected Weyl points on the sample surface plane. **c**, ±1st grating order excited bulk bands within the range of $k_x \in [-100k_0, 100k_0]$ (+1st bands are indicated with navy color and -1st with purple) and surface states for $\varphi = 30°$ on the $B$ - $f$ plane. Here we set $\gamma = 0$. **d**, Simulated reflection spectra for $\varphi = 30°$, $h$=10000 μm, as well as the calculated surface states (black dashed) under ±1st grating order excitation~~ and the~~

~~cyclotron line (red dashed)~~. **e**, Experimentally measured reflection spectra for $\varphi = 30°$, $h$=1250 µm. **f-h**, Similar to **c-e** but for $\varphi = 45°$.

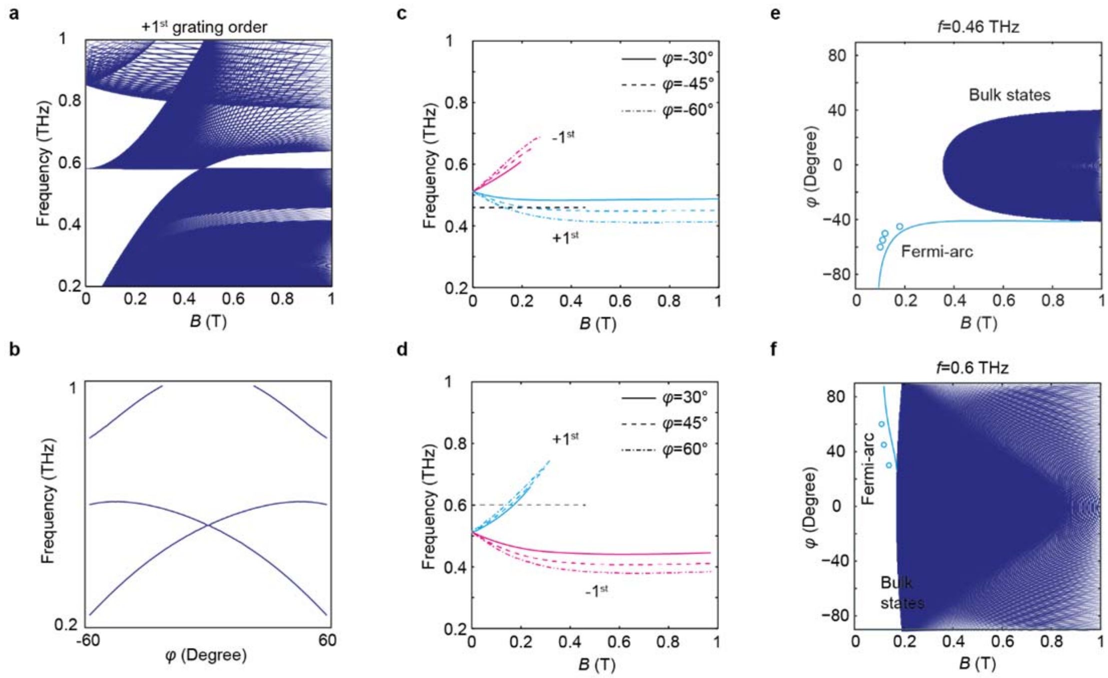


**Figure 4 | Photonic Weyl points and Fermi-arcs in synthetic space.** **a**, Projected band along $k_x$ axis on the $f$ - $B$ plane, within the range of $k_x \in$ [-100$k_0$, 100$k_0$] for $\varphi$=0°, the Weyl point can be found around B=0.472 T. **b**, The linear dispersion along $\varphi$. **c**, ±1$^{st}$ order grating selected surface state on $B$ - $f$ plane for $\varphi$=−30°, -45°, -60°. **d**, Similar to **c** but for $\varphi$=30°, 45°, 60°. **e**, Constructed photonic Fermi-arcs on ($B$, $\varphi$) space for frequency of $f$=0.46 THz, within the range of $k_x \in$ [-100$k_0$, 100$k_0$]. **f**, Similar to **e** but for $f$=0.6 THz. Cyan hollow dots indicate experimentally measured results.

## References:


1 Wan, X., Turner, A. M., Vishwanath, A. & Savrasov, S. Y. Topological semimetal and Fermi-arc surface states in the electronic structure of pyrochlore iridates. *Physical Review B* **83**, 205101, doi:10.1103/PhysRevB.83.205101 (2011).

2 Burkov, A. A. & Balents, L. Weyl Semimetal in a Topological Insulator Multilayer. *Physical Review Letters* **107**, 127205, doi:10.1103/PhysRevLett.107.127205 (2011).

3 Xu, G., Weng, H., Wang, Z., Dai, X. & Fang, Z. Chern Semimetal and the Quantized Anomalous Hall Effect in $HgCr_2Se_4$. *Physical Review Letters* **107**, 186806, doi:10.1103/PhysRevLett.107.186806 (2011).

4 Lu, L., Fu, L., Joannopoulos, J. D. & Soljačić, M. Weyl points and line nodes in gyroid photonic crystals. *Nature Photonics* **7**, 294, doi:10.1038/nphoton.2013.42 https://www.nature.com/articles/nphoton.2013.42#supplementary-information (2013).

5 Xu, S.-Y. *et al.* Discovery of a Weyl fermion semimetal and topological Fermi arcs. *Science* **349**, 613 (2015).

6 Weng, H., Fang, C., Fang, Z., Bernevig, B. A. & Dai, X. Weyl Semimetal Phase in Noncentrosymmetric Transition-Metal Monophosphides. *Physical Review X* **5**, 011029, doi:10.1103/PhysRevX.5.011029 (2015).

7 Lu, L. *et al.* Experimental observation of Weyl points. *Science* **349**, 622 (2015).

8 Soluyanov, A. A. *et al.* Type-II Weyl semimetals. *Nature* **527**, 495, doi:10.1038/nature15768 https://www.nature.com/articles/nature15768#supplementary-information (2015).

9 Huang, L. *et al.* Spectroscopic evidence for a type II Weyl semimetallic state in $MoTe_2$. *Nature Materials* **15**, 1155, doi:10.1038/nmat4685 (2016).

10 Lin, Q., Xiao, M., Yuan, L. & Fan, S. Photonic Weyl point in a two-dimensional resonator lattice with a synthetic frequency dimension. *Nature Communications* **7**, 13731, doi:10.1038/ncomms13731 https://www.nature.com/articles/ncomms13731#supplementary-information (2016).

11 Chang, G. *et al.* Room-temperature magnetic topological Weyl fermion and nodal line semimetal states in half-metallic Heusler $Co_2TiX$ (X=Si, Ge, or Sn). *Scientific Reports* **6**, 38839, doi:10.1038/srep38839 (2016).

12 Wang, Z. *et al.* Time-Reversal-Breaking Weyl Fermions in Magnetic Heusler Alloys. *Physical Review Letters* **117**, 236401, doi:10.1103/PhysRevLett.117.236401 (2016).

13 Kübler, J. & Felser, C. Weyl points in the ferromagnetic Heusler compound $Co_2MnAl$. *EPL (Europhysics Letters)* **114**, 47005 (2016).

14 Wang, Q., Xiao, M., Liu, H., Zhu, S. & Chan, C. T. Optical Interface States Protected by Synthetic Weyl Points. *Physical Review X* **7**, 031032, doi:10.1103/PhysRevX.7.031032 (2017).

15 N.P. Armitage, E. J. M., Ashvin Vishwanath. Weyl and Dirac semimetals in three-dimensional solids. *Reviews of Modern Physics* **90**, 015001, doi:10.1103/RevModPhys.90.015001 (2018).

16 Ozawa, T. *et al.* Topological Photonics. *arXiv:1802.04173 [physics.optics]* (2018).

17 Borisenko, S. *et al.* Time-reversal symmetry breaking Type-II Weyl state in $YbMnBi_2$. *arXiv:1507.04847 [cond-mat.mes-hall]* (2015).

18 Liu, E. *et al.* Giant anomalous Hall effect in a ferromagnetic kagome-lattice semimetal. *Nature Physics* **14**, 1125, doi:10.1038/s41567-018-0234-5 (2018).

19 Gao, W. *et al.* Photonic Weyl degeneracies in magnetized plasma. *Nature Communications* **7**, 12435, doi:10.1038/ncomms12435 https://www.nature.com/articles/ncomms12435#supplementary-information (2016).

20 Cheng, X. *et al.* Robust reconfigurable electromagnetic pathways within a photonic topological insulator.

*Nature Materials* **15**, 542, doi:10.1038/nmat4573 https://www.nature.com/articles/nmat4573#supplementary-information (2016).

21 Tan, W., Chen, L., Ji, X. & Lin, H.-Q. Photonic simulation of topological superconductor edge state and zero-energy mode at a vortex. *Scientific Reports* **4**, 7381, doi:10.1038/srep07381 (2014).

22 Jin, D. *et al.* Topological magnetoplasmon. *Nature Communications* **7**, 13486, doi:10.1038/ncomms13486 https://www.nature.com/articles/ncomms13486#supplementary-information (2016).

23 Goi, E., Yue, Z., Cumming, B. P. & Gu, M. Observation of Type I Photonic Weyl Points in Optical Frequencies. *Laser & Photonics Reviews* **12**, 1700271, doi:10.1002/lpor.201700271 (2018).

24 Chen, W.-J., Xiao, M. & Chan, C. T. Photonic crystals possessing multiple Weyl points and the experimental observation of robust surface states. *Nature Communications* **7**, 13038, doi:10.1038/ncomms13038 https://www.nature.com/articles/ncomms13038#supplementary-information (2016).

25 Yang, B. *et al.* Direct observation of topological surface-state arcs in photonic metamaterials. *Nature Communications* **8**, 97, doi:10.1038/s41467-017-00134-1 (2017).

26 Yang, B. *et al.* Ideal Weyl points and helicoid surface states in artificial photonic crystal structures. *Science* **359**, 1013, doi:10.1126/science.aaq1221 (2018).

27 Noh, J. *et al.* Experimental observation of optical Weyl points and Fermi arc-like surface states. *Nature Physics* **13**, 611, doi:10.1038/nphys4072 https://www.nature.com/articles/nphys4072#supplementary-information (2017).

28 O'Brien, T. E., Diez, M. & Beenakker, C. W. J. Magnetic Breakdown and Klein Tunneling in a Type-II Weyl Semimetal. *Physical Review Letters* **116**, 236401, doi:10.1103/PhysRevLett.116.236401 (2016).

29 Liu, C.-X., Ye, P. & Qi, X.-L. Chiral gauge field and axial anomaly in a Weyl semimetal. *Physical Review B* **87**, 235306, doi:10.1103/PhysRevB.87.235306 (2013).

30 Kharzeev, D. E., Kikuchi, Y., Meyer, R. & Tanizaki, Y. Giant photocurrent in asymmetric Weyl semimetals from the helical magnetic effect. *Physical Review B* **98**, 014305, doi:10.1103/PhysRevB.98.014305 (2018).

31 Yang, Z. *et al.* Weyl points in a magnetic tetrahedral photonic crystal. *Opt. Express* **25**, 15772-15777, doi:10.1364/OE.25.015772 (2017).

32 Wang, Z., Chong, Y., Joannopoulos, J. D. & Soljačić, M. Observation of unidirectional backscattering-immune topological electromagnetic states. *Nature* **461**, 772, doi:10.1038/nature08293 https://www.nature.com/articles/nature08293#supplementary-information (2009).

33 Poo, Y., Wu, R.-x., Lin, Z., Yang, Y. & Chan, C. T. Experimental Realization of Self-Guiding Unidirectional Electromagnetic Edge States. *Physical Review Letters* **106**, 093903, doi:10.1103/PhysRevLett.106.093903 (2011).

34 Morozov, A. I. *Introduction to Plasma Dynamics*. (CRC Press, 2012).

35 Zhang, S., Xiong, Y., Bartal, G., Yin, X. & Zhang, X. Magnetized Plasma for Reconfigurable Subdiffraction Imaging. *Physical Review Letters* **106**, 243901, doi:10.1103/PhysRevLett.106.243901 (2011).

36 Yang, B., Lawrence, M., Gao, W., Guo, Q. & Zhang, S. One-way helical electromagnetic wave propagation supported by magnetized plasma. *Scientific Reports* **6**, 21461, doi:10.1038/srep21461 (2016).

37 Gangaraj, S. A. H. & Monticone, F. Topological waveguiding near an exceptional point: defect-immune, slow-light, and loss-immune propagation. *Physical review letters* **121**, 093901 (2018).

38 Gangaraj, S. *et al.* Truly unidirectional excitation and propagation of diffractionless surface plasmon-polaritons. *arXiv preprint arXiv:1811.00463* (2018).

39 Howells, S. C. & Schlie, L. A. Transient terahertz reflection spectroscopy of undoped InSb from 0.1 to 1.1 THz.

*Applied Physics Letters* **69**, 550-552, doi:10.1063/1.117783 (1996).

40 Wang, X., Belyanin, A. A., Crooker, S. A., Mittleman, D. M. & Kono, J. Interference-induced terahertz transparency in a semiconductor magneto-plasma. *Nature Physics* **6**, 126, doi:10.1038/nphys1480 https://www.nature.com/articles/nphys1480#supplementary-information (2009).

41 Zhang, Q. *et al.* Superradiant decay of cyclotron resonance of two-dimensional electron gases. *Physical review letters* **113**, 047601 (2014).